# Supporting Information for "What are the causes of tropical cirrus longwave biases in global storm-resolving simulations?"

R.L. Atlas[1], C.S. Bretherton[2], A.B. Sokol[1], P.N. Blossey[1], M.F. Khairoutdinov[3]

[1]Dept. of Atmospheric Sciences, University of Washington, Seattle, WA

[2]Allen Institute for Artificial Intelligence, Seattle, WA

[3]School of Marine and Atmospheric Sciences, Stony Brook University, Stony Brook, NY

[1]3920 Okanogan Ln, Seattle, WA 98195

[2]2157 N Northlake Way #110, Seattle, WA 98103

[3]Endeavour, 145, Stony Brook, NY 11790

## Contents of this file

1. Text S1 to S3
2. Figures S1 to S3

## Additional Supporting Information (File uploaded separately)

1. Caption for Movie S1

**Text S1: Description of ice microphysics in the four different microphysics schemes**

In SAM1MOM (Khairoutdinov & Randall, 2003), two prognostic variables represent all water species: (1) total water mass mixing ratio, which combines water vapor and non-precipitating hydrometeors and (2) the precipitating hydrometeor mass mixing ratio. Both non-precipitating (cloud liquid and cloud ice) and precipitating (rain, snow and graupel) hydrometeors are partitioned between liquid and ice phases based on temperature, and ice phase precipitating hydrometeor mass is further partitioned between snow and graupel based on temperature. Only cloud ice is radiatively active. SAM1MOM partitions total water into water vapor and cloud condensate using saturation adjustment at all temperatures, including for cloud ice. This means that cloud ice condenses and sublimates instantaneously at ice saturation. M2005 (Morrison et al., 2005) predicts number and mass for three frozen hydrometeor classes (cloud ice, snow and graupel), and cloud ice and snow are both radiatively active. Thompson (Thompson et al., 2008) predicts mass for three frozen hydrometeor classes (cloud ice, snow and graupel) and number for cloud ice only. Snow number is prescribed as a function of snow mass and temperature. Cloud ice and snow are both radiatively active. P3 (Morrison & Milbrandt, 2015) is run with one radiatively active ice class, for which it predicts mass, number, rime volume and rime mass.

M2005, Thompson and P3 heterogeneously nucleate ice through deposition and immersion freezing. M2005 also includes contact nucleation. At the temperatures and heights examined here, deposition nucleation dominates heterogeneous nucleation.

In M2005, deposition nucleation occurs when either ice supersaturation exceeds 8% or the air is saturated with respect to liquid and colder than $-12°$C. In Thompson, it occurs when either ice supersaturation exceeds 25% or air is saturated with respect to liquid and colder than $-12°$C.

In P3, it occurs when the temperature is below $-15°$C and ice supersaturation exceeds 5%. All three schemes use the Cooper curve (Cooper, 1986) to specify the concentration of ice nucleating particles for deposition nucleation and have limiters which specify a maximum concentration of ice particles that can be formed by deposition nucleation. The limiters in P3, M2005, and Thompson are .1, .25 and .5 $cm^{-3}$, respectively.

All three microphysics schemes also support homogeneous freezing of droplets and raindrops when the air temperature is $< -40°$C but do not support homogeneous freezing of aerosol. Limiters act to restrict the total concentrations of cloud ice particles to be no larger than 2, .3 and .25 $cm^{-3}$ in P3, M2005 and Thompson, respectively.

**Text S2: Processing of DARDAR and 2C-ICE**

DARDAR and 2C-ICE both retrieve frozen water content (FWC) from Cloud-Aerosol Lidar and Infrared Pathfinder Satellite Observation (CALIPSO) lidar attenuated backscatter and CloudSat radar reflectivity. A major difference between the two retrievals is that 2C-ICE parameterizes radar reflectivity for grid cells where the cloud is too thin to be detected by the CloudSat radar (Deng et al., 2015). Here, we compare retrievals of frozen water content (FWC) and frozen water path (FWP) between DARDAR V3.10 and 2C-ICE to examine the impact of that difference. Because the two versions of DARDAR are more similar to each other than they are to the 2C-ICE, we only examine the newer version of DARDAR here.

Figure S1 shows distributions of FWC from the two satellite retrievals broken up into daytime and nighttime measurements, and, in the bottom three rows, according to which instruments the retrieval is coming from (lidar only, radar only or both). In general, retrieved FWCs are smaller in 2C-ICE than in DARDAR. Most of this differences comes from lidar-only regions, where 2C-

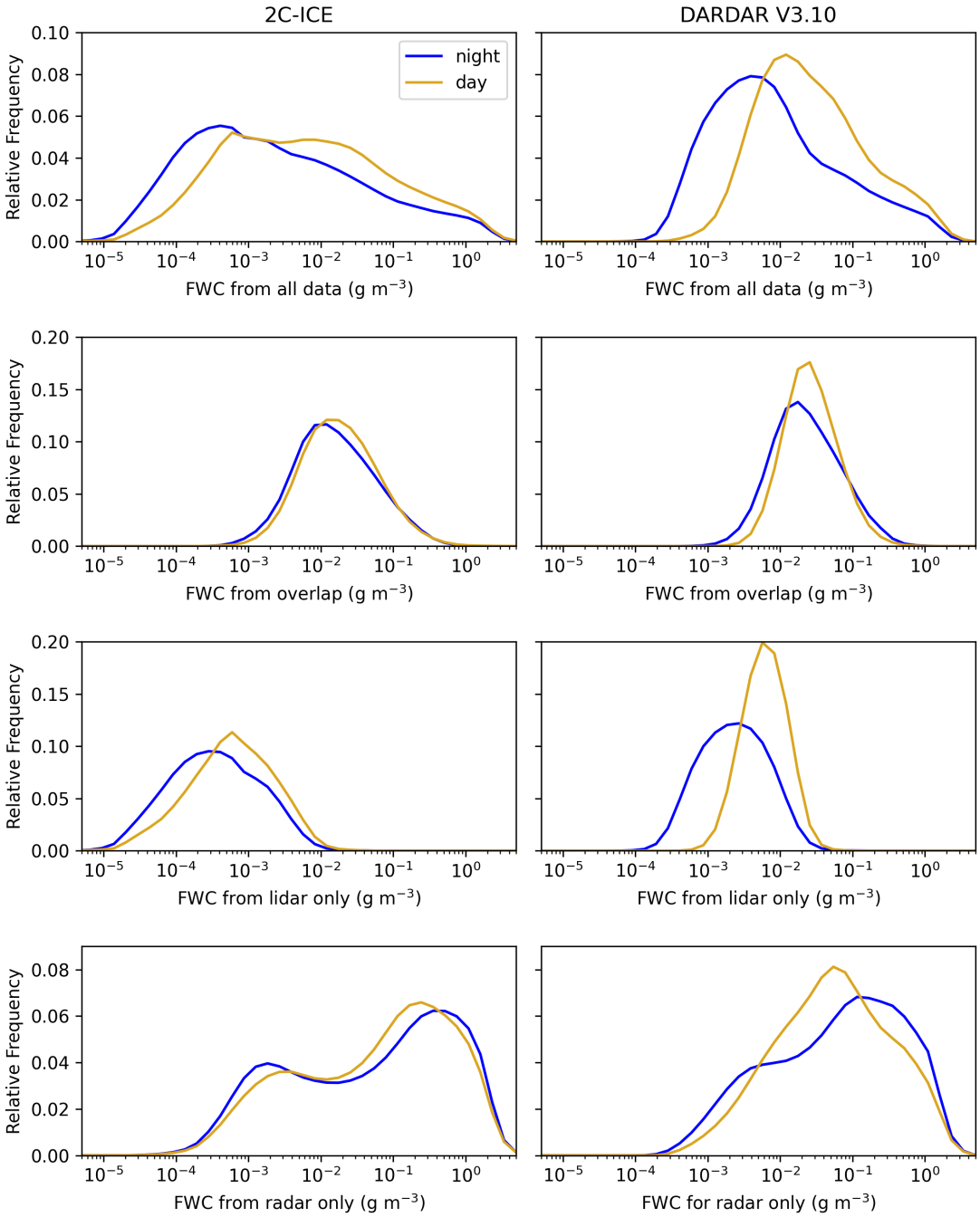


**Figure S1.** Distributions of FWC from nighttime and daytime measurements separately for (top to bottom row) all data, regions sensed by both the radar and lidar, lidar only regions, and radar only regions, for 2C-ICE (left) and DARDAR (right).

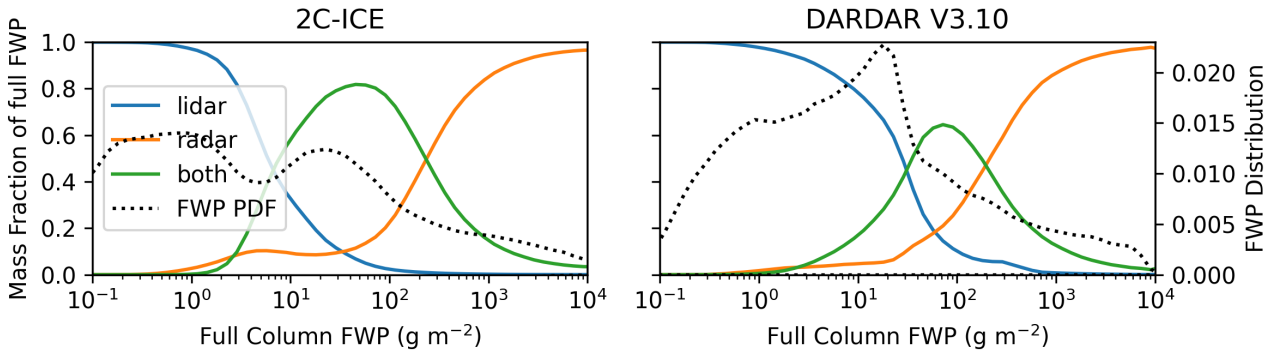


**Figure S2.** Blue, orange and green lines show the average mass fraction of a column that is sensed by the lidar only, radar only, and both instruments, respectively, as a function of column FWP.

ICE returns FWCs that are one order of magnitude smaller on average than those retrieved by DARDAR. 2C-ICE also has a more bimodal distribution than DARDAR for radar-only regions. The two retrievals agree best for regions with both instruments.

DARDAR's retrievals show a greater diurnal dependence, particular in the lidar-only regions, due to the fact that the lidar is more sensitive at night. Because DARDAR has greater sensitivity at night, we restrict our comparisons between the simulations and satellite retrievals to nighttime measurements. Additionally, because DARDAR cannot detect FWCs $< 10^{-4}$ g m$^{-3}$ at night, we filter FWCs smaller than that out of both the simulated output and the satellite retrievals before computing FWP.

Given that the retrievals diverge most from each other in lidar only regions, we examine the mass fraction that comes from lidar-only regions, radar-only regions and regions with both instruments as a function of FWP in Figure S2 (left y-axis). Distributions of FWP are overlaid (right y-axis). For FWPs $> 30$ g m$^{-2}$, most of the FWP comes from regions with both instruments

or with radar only. Accordingly, the two retrievals agree well within this range. For FWPs $< 30$ g m$^{-2}$, the satellite retrievals are very different from each other and do not provide as tight a constraint on the simulations.

**Text S3: Processing of the Microphysics Guide**

The Microphysics Guide (Krämer, Rolf, Spelten, Afchine, et al., 2020; Krämer, Rolf, & Spelten, 2020) includes quality controlled microphysics and thermodynamics observations from 24 field campaigns. Five of those campaigns measured FWC and ice crystal number concentration ($N_{ice}$) at latitudes between 20°S and 20°N and altitudes $> 10$ km, including Airborne Tropical TRopopause EXperiment (Jensen et al., 2017, ATTREX), Convective Transport of Active Species in the Tropics EXperiment (Pan et al., 2017, CONTRAST), Aerosol, Cloud, Precipitation, and Radiation Interactions and Dynamics of Convective Cloud Systems (Wendisch et al., 2016, ACRIDICON), Tropical Composition, Cloud and Climate Coupling Experiment (Toon et al., 2010, TC4), and Pacific Oxidants, Sulfur, Ice, Dehydration, and cONvection (POSIDON). Figure S3 shows the flight tracks from all five campaigns, and lists the instruments used to measure or compute FWC and $N_{ice}$.

All data in the Microphysics Guide has a resolution of 1 Hz. Air speeds in the upper troposphere are typically 200 m s$^{-1}$, so we coarsened the data to .04 Hz (or 25 seconds) so that each data point would correspond to an approximately 5 km horizontal distance, and better match the spacial scale of the simulated output. The numbers next to the flight campaign names in Figure S3 are the number of .04 Hz in-cloud data points that match the latitude and altitude criteria.

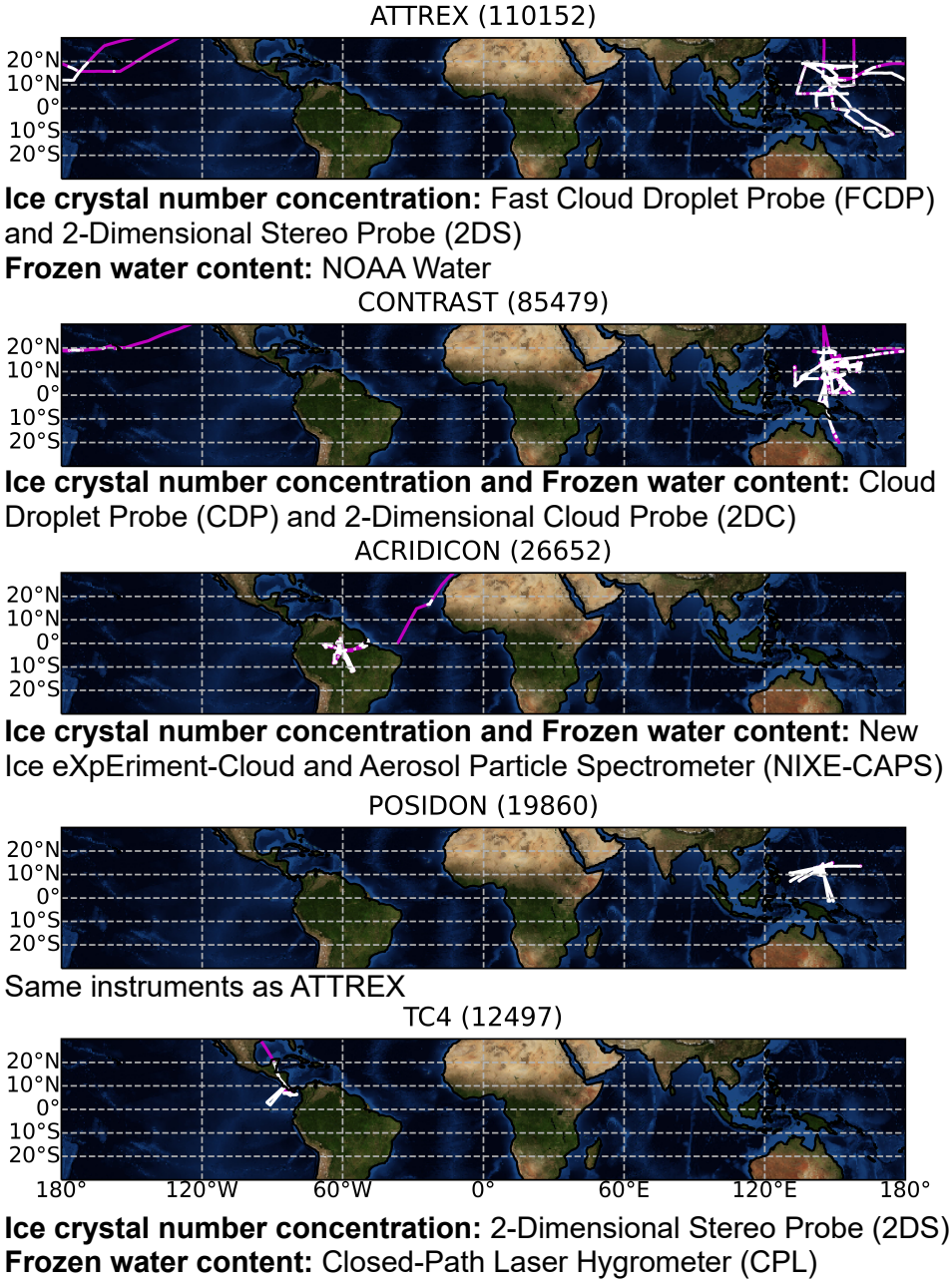


**Figure S3.** Campaign flight tracks in magenta with white overlay indicating in-cloud data above 10 km and within 20°N and 20°S. Map titles include the campaign name and the number of .04 Hz data points used in parentheses. Below each map, instruments used to measure or compute FWC and $N_{ice}$ are listed.

**Movie S1.** For each hour of output from days 2-5 of the simulations, we show **left:** Snapshots of simulated frozen water path (FWP, including cloud ice, snow and graupel) for columns with cloud top height (CTH) $> 10$ km on the simulations' native grid and **right:** Coincident snapshots of longwave CRE bias compared to CERES on a coarsened $1^\circ$ x $1^\circ$ grid. At high zenith angles, CERES sometimes mistakes land for cloud, causing a positive (blue) bias over the land. This is especially evident over Africa.